ARTICLE

Atomic-scale Insight into Enhanced Surface Stability of Methylammonium Lead Iodide Perovskite by Controlled Deposition of Lead Chloride

Received 00th January 20xx,
Accepted 00th January 20xx

DOI: 10.1039/x0xx00000x

Afshan Jamshaid [†, a], Zhendong Guo [†, b], Jeremy Hieulle [a], Collin Stecker [a], Robin Ohmann [a, ‡], Luis K. Ono [a], Longbin Qiu [a], Guoqing Tong [a], Wanjian Yin [*, b], and Yabing Qi [*, a]

Incorporation of a certain amount of Cl ions into methylammonium lead iodide ($MAPbI_3$) perovskite films and how these incorporated Cl ions affect the structural and electronic properties of these films have been an intensively studied topic. In this study, we comprehensively investigated Cl incorporation in $MAPbI_3$ at the atomic scale by a combined study of scanning tunneling microscopy, X-ray photoelectron spectroscopy, ultraviolet and inverse photoemission spectroscopy, density functional theory and molecular dynamics calculations. At a Cl concentration of $14.8 \pm 0.6\%$, scanning tunneling microscopy images confirm the incorporation of Cl ions on the $MAPbI_3$ surface, which also corresponds to the highest surface stability of $MAPbI_3$ found from the viewpoint of both thermodynamics and kinetics by density functional theory and molecular dynamics calculations. Our results show that the Cl concentration is crucial to the surface bandgap and stability of $MAPbI_3$.

Introduction

Pioneering works have demonstrated that metal halide perovskites (ABX_3, A is methylammonium (MA^+); B is Pb^{2+}; X is I^-, Br^-, Cl^-.) as the light harvest layer show a great potential in solar cell applications [1 3]. In the past decade, perovskite solar cells (PSCs) have attracted immense research interest, due to the rapid increase in efficiencies from 3.8% [1] to 25.5% [2] and low-cost fabrication. The advantages of perovskites in solar cell applications include facile fabrication, high absorption coefficient, bandgap tunability, low non-radiative recombination rates, and long charge carrier diffusion lengths. However, perovskites undergo relatively fast degradation dynamics under external stimulus such as elevated temperature, UV-light, oxygen, moisture, built-in electric field, and interfacial chemical reactions [3].

To enhance the intrinsic stability of perovskites, mixing of halide anions (I, Br, Cl) at the X site of the perovskite ABX_3 structure has been proposed [4-5 6]. As an example, it has been suggested that mixing $MAPbI_3$ with Cl could greatly improve the stability of the perovskite material against moisture, thermal heat, and light [7 8]. Furthermore, Cl incorporation to the perovskite film has shown to be an effective strategy to enhance power conversion efficiencies (PCEs) of the perovskite solar cell device [8]. Stergiopoulos and co-workers showed that the $MAPbI_3$ perovskite films incorporated with Cl exhibited good light-harvesting capabilities, and the absorption spectra were stable against prolonged light exposure, as demonstrated by 1000 hours of constant illumination under simulated full sunlight [9]. Cl incorporation in the perovskite precursor solution was reported to improve $MAPbI_3$ optoelectronic properties, *e.g.*, diffusion lengths for electrons and holes of ~130 nm and ~90-105 nm in $MAPbI_3$ increased by approximately 10 times in $MAPb(I_{1-x}Cl_x)_3$, to ~1069 nm and ~1213 nm, respectively [10 11 12]. Similarly, it is found that partial substitution of iodine ions by chlorine in α-$FAPbI_3$ [13] and α-$CsPbI_3$ perovskites enhances the interaction between the PbX_6 octrahedra and the cations at the "A" sites as well as the bonding between Pb and halides explained by the higher electronegativity of Cl [14 15 16 17]. Furthermore, the addition of Cl in more complex perovskite compositions of mixed cations (MACsFA) and halides (I, Br) led to remarkable optoelectronic properties with a two-fold increase in photocarrier lifetime and charge carrier mobility [14]. This triple halide (I, Br, Cl) perovskites also showed suppressed light-induced phase segregation even at 100-sun illumination and <4% degradation when integrated into a solar cell device (initial PCE of 20.42%) operated at the maximum power point for 1000 hours [14]. Despite the tremendous advantages provided by Cl incorporation for enhancing perovskite optoelectronic properties and stability, the question how Cl is incorporated in$MAPbI_3$ is still a topic under debate [18].

Several reports proposed that Cl was absent in the final $MAPbI_3$ film or its concentration was below the detection limits of the analytical instruments [19]. Therefore, the Cl-containing compounds (*e.g.*, MACl, $PbCl_2$) were considered as additives that mainly improved $MAPbI_3$ film morphology [20 21 22 18 23]. However, some studies based on X-ray diffraction (XRD) and absorption spectroscopy[24 25], indicate that although most of Cl leaves the final perovskite film during the post-annealing process, a small amount of Cl is incorporated in the

[a] *Energy Materials and Surface Sciences Unit (EMSSU), Okinawa Institute of Science and Technology Graduate University (OIST), 1919-1 Tancha, Onna-son, Okinawa 904-0495, Japan.*
[b] *College of Energy, Soochow Institute for Energy and Materials Innovations (SIEMIS) and Jiangsu Provincial Key Laboratory for Advanced Carbon Materials and Wearable Energy Technologies, Soochow University, Suzhou 215006, China.*
[†] *These authors contributed equally to this work.*
*Corresponding authors: Yabing Qi, Yabing.Qi@OIST.jp; Wanjian Yin, wjyin@suda.edu.cn.
[‡] Current address: Department Physik, Universität Siegen, 57068 Siegen, Germany.
Electronic Supplementary Information (ESI) available: [details of any supplementary information available should be included here]. See DOI: 10.1039/x0xx00000x

$MAPbI_3$ film. Based on density functional theory (DFT) calculations, Mosca and co-workers reported that a maximum amount of Cl in the bulk of $MAPbI_3$ is 3-4% [26]. Early theoretical calculations suggested a small amount of Cl may exist at grain boundaries and play a role in defect passivation [27]. Although it is generally accepted that a small amount of Cl can be incorporated in $MAPbI_3$, a consensus has not been reached regarding the location of the residual Cl in the perovskite lattice [10] [28]. In the past few years, scanning tunnelling microscopy (STM) has been used to study the surface structure and electronic properties of perovskite materials down to the atomic level [29] [30] [31] [32] [33] [34] [35]. The real space atomic resolution of STM made it a technique of choice for unrevealing the location of Cl ions in the perovskite film.

In this work, for the first time we determine the configuration of Cl incorporation in the surface lattice of the $MAPbI_3$ ultra-thin film (~4-5 nm). By using STM with the assistance of density functional theory (DFT) and molecular dynamics calculations, we show with atomic-scale precision the exact location of the Cl ions on the surface of the perovskite film. X-ray photoelectron spectroscopy (XPS) was used to measure the perovskite film surface composition, while ultraviolet photoemission spectroscopy (UPS) and inverse photoemission spectroscopy (IPES) were used to show the impact of the Cl incorporation on the surface electronic properties of the $MAPbI_3$film. We found that the incorporation of Cl ions on the $MAPbI_3$ surface significantly alters its electronic properties, by widening the bandgap of $MAPbI_3$ from 1.13 eV to 1.62 eV. Perovskite bandgap plays a key role in light harvesting and stability [14] of PSCs. For single junction solar cells, the bandgap from 1.3 eV to 1.4 eV is ideal [36], while for two-junction tandem solar cells the wider bandgap is desirable [14]. Thus, bandgap tuning by Cl incorporation in $MAPbI_3$ can potentially make it a more suitable choice as the top cell in a tandem solar cell. Moreover, from the theoretical point, the larger bandgap means the weaker non-radiative charge recombination and longer carrier lifetime [37]. The surface contributes to a large portion of carrier recombination in $MAPbI_3$ [38] [39]. Incorporation of a suitable amount of Cl not only passivates the recombination centers [41] [42], but also opens a larger gap at the surface [30], which may help create a type-I straddling band alignment [40] so that electrons and holes may not easily meet each other at the surface.

At last, we determined the optimal Cl concentration corresponding to the enhanced stability of $MAPbI_3$ surfaces. Similar to our previous STM works [30] [29], it is important to point out that although STM enables atomic-resolution imaging in real space, it is a surface-sensitive characterization technique. Therefore, STM combined with DFT calculations can be employed to investigate the structures and properties of the surface but not the bulk. In addition, in this study, we used UPS and IPES to study electronic properties of the sample surface. The probing depth of UPS and IPES is between 2 nm and 6 nm. Therefore, the findings presented in this work are mainly surface science-relevant and it is nontrivial to make a direct connection with the bulk film in a solar cell device. Nevertheless, our surface science results provide valuable insights into surface/interface properties of perovskite materials, which play an important role in determining the performance of perovskite solar cells [43] [44]. Studies have shown that the interface between the charge selective layer and perovskite film is crucial for achieving high performance solar cells [9] [44] [45] [46]. Therefore, the major aim of our current surface science study is to examine the atomic scale surface structures and electronic properties, which are important for understanding the underlying mechanisms behind: (i) Cl diffusion into the perovskite film [47] [48] [49] and (ii) passivation of surface defects by Cl [41] [50].

Results

The $MAPbI_3$ films (~4-5 nm) were grown on Au (111) single crystal substrates by *in situ* thermal evaporation in ultra-high vacuum (UHV) following the previously reported recipe (see **Methods** Section) [34]. The UHV grown pristine and Cl incorporated $MAPbI_3$ films show a polycrystalline nature composed of multiple grains with typical grain sizes varying from 8 nm to 15 nm (**Fig S1a-b**). Within a grain, the perovskite surface shows two different structures, i.e., the dimer and zigzag structures (**Figs 1a-c, and Fig S2a**), as previously observed for $MAPbI_3$ films [33] [34]. In the dimer structure, the formation of I-I pairs was found, which is a result of the reorientation of MA cations [34]. Such configurations were also observed in both thin film samples and single crystal samples of $MAPbBr_3$ [30-32]. To achieve the incorporation of Cl ions in the perovskite film, 4 different evaporation times (see **Methods** Section) of $PbCl_2$ were explored. First, we deposited $PbCl_2$ for 1 min onto the pristine $MAPbI_3$ thin film but Cl incorporation was not observed according to XPS measurements. After increasing the evaporation time of $PbCl_2$ to 4 min (**Fig S2b-c)** and 6 min, darker protrusions with a lower apparent height and smaller diameter started to appear in the STM images (dashed ellipses in **Figs 1d,e**). The deposition thickness was estimated by depositing $PbCl_2$ for 4 min directly on a clean Au (111) surface, which corresponds to the 0.5 monolayer (ML) sample coverage determined by STM measurements. On the basis of the 0.5 ML coverage case, we have estimated the coverage of 0.75 ML for a deposition time of of 6 min, and the coverage of 1.5 ML for a deposition time of 12 min.

We prepared a total of 7 samples and that the results were reproducible for the 0.75 ML of $PbCl_2$ on $MAPbI_3$. **Fig 2** shows the histogram of the apparent height distribution observed at the surface of $MAPbI_3$ perovskite after Cl incorporation (0.75 ML of $PbCl_2$). The determination of the surface concentration of Cl in $MAPbI_3$ was carefully analysed because the surface inhomogeneity of Cl in $MAPbI_3$ was previously reported [51]. The protrusion statistics were obtained from 12 STM images acquired on different macroscopic areas of the same sample and are consistent from sample to sample (7 samples in total). The comparison of the pristine and Cl incorporated dimer and zigzag structures is shown in **Fig 3**. The distribution of the STM apparent height values for the protrusions observed in these STM images (approximately 900 protrusions)

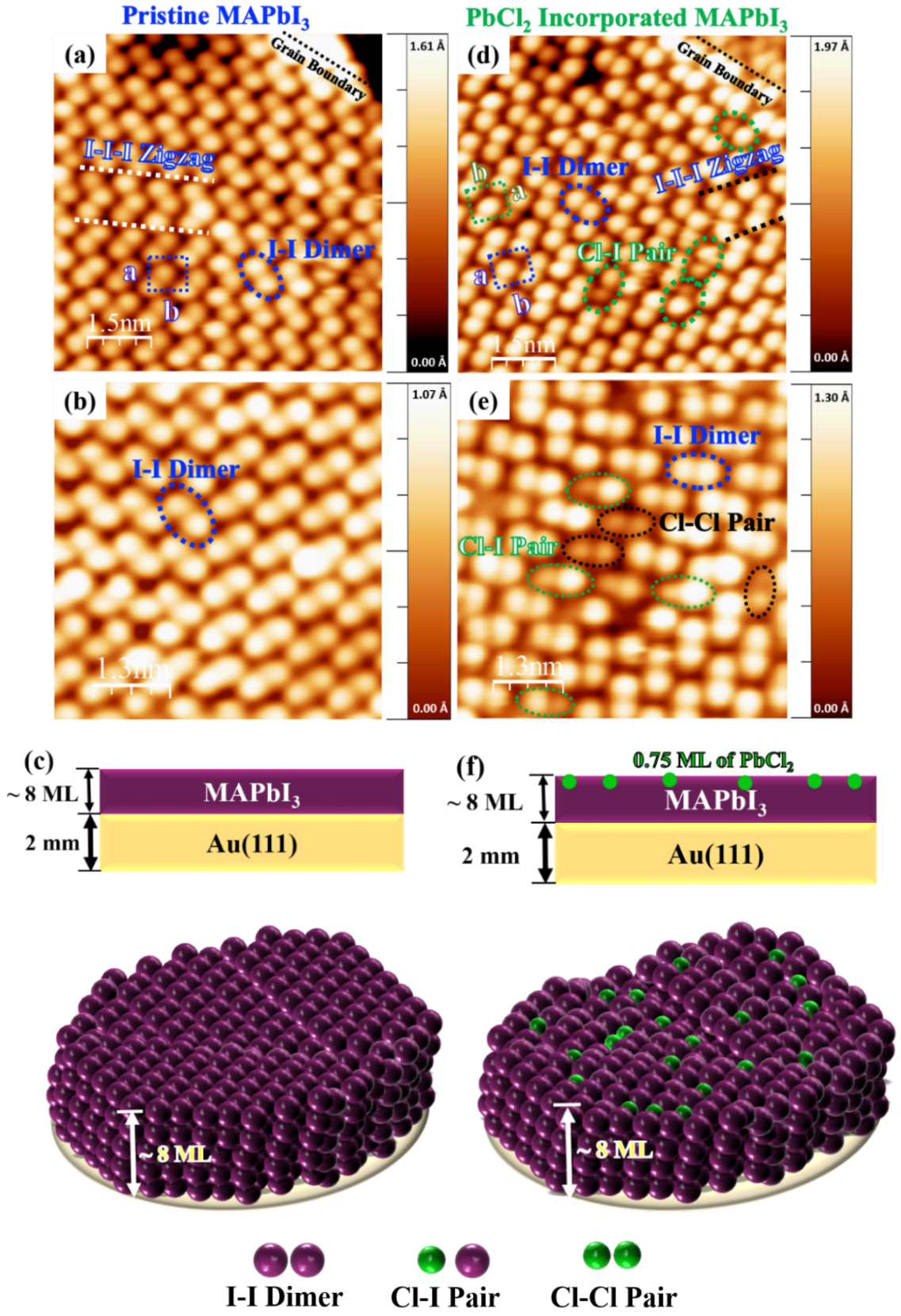

Fig 1. LT-STM images of the surface of the pristine $MAPbI_3$ perovskite thin film and the 0.75 ML of $PbCl_2$ incorporated $MAPbI_3$ perovskite thin film deposited on Au (111). (a-b) I-I dimer (blue dashed ellipses) and I-I-I zigzag structures (white dashed lines) on the pristine $MAPbI_3$ thin film surface (Scan area = 14 × 14 nm^2; Sample bias voltage = –2.5 V; Tunnelling current = 50 pA) with the unit cell (blue dashed square). (c) Atomic model configuration of pristine $MAPbI_3$ on Au (111). (d-e) I-I dimers and Cl incorporated Cl-I pair structures (green dashed ellipses) in the centre, close to the grain boundary (green dashed line), inside a grain (Scan area = 14.5 × 14.5 nm^2; Sample bias voltage = –2.5 V; Tunnelling current = 50 pA) with the unit cell (green dashed square) and Cl-Cl pair (black dashed ellipses). (f) Atomic model configuration of 0.75 ML of $PbCl_2$ incorporated $MAPbI_3$ on Au (111).

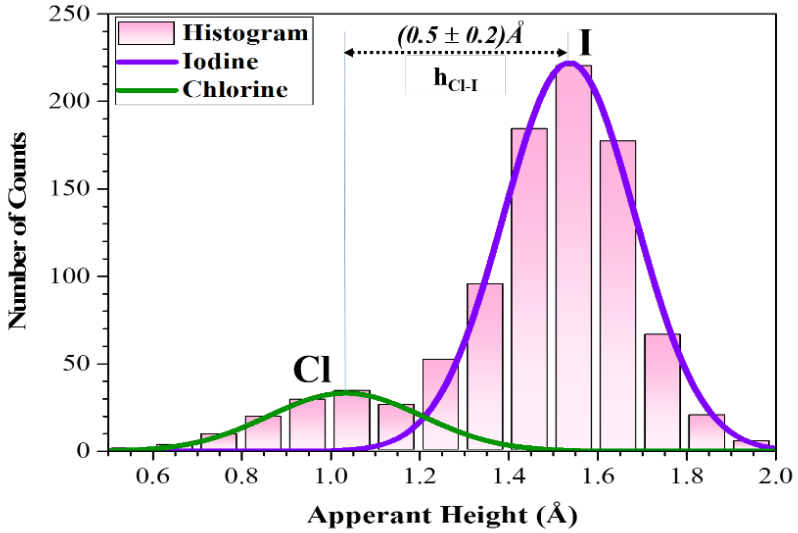

Fig 2. Histogram of the apparent height distribution of I and Cl anions. The surface concentration in $MAPbI_3$ is 14.8 ± 0.6%, which was obtained from the statistical analyses on the basis of 900 data points.

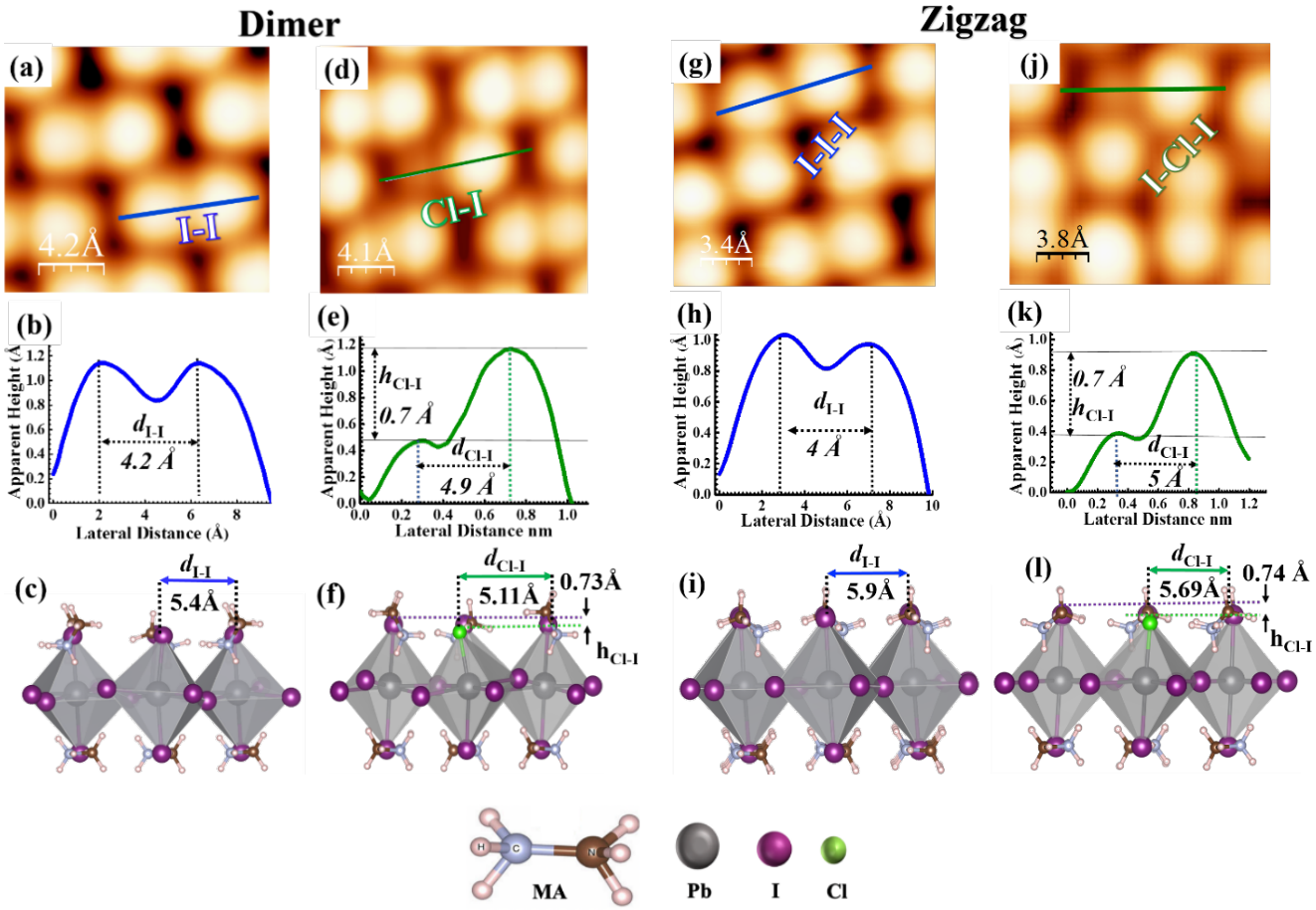

Fig 3. STM images of pristine and Cl incorporation in a dimer and zigzag structure of $MAPbI_3$ (a) High-resolution STM image showing an I-I dimer structure (Scan area = 18 × 18 Å^2; Sample bias voltage = –2.50 V, Tunneling current = 20 pA). (b) Height profile and bond length of the observed I-I dimer in (a). (c) DFT simulated height profile and bond length for the I-I dimer in (a). (d) High-resolution STM image showing one Cl ion that forms a pair with one I ion in a dimer structure (Scan area = 18 × 18 Å^2; Sample bias voltage = –2.50 V, Tunneling current = 20 pA). (e) Height profile and bond length of the observed Cl-I pair in (d). (f) DFT simulated height profile and bond length for the Cl-I pair in (d). (g) High-resolution STM image showing I-I-I that forms a zigzag structure (Scan area = 15 × 15 Å^2; Sample bias voltage = –2.50 V, Tunneling current = 20 pA). (h) Height profile and bond length of the observed I-I zigzag structure in (g). (i) DFT simulated height profile and bond length of the observed I-I zigzag structure in (g). (j) High-resolution STM image showing one Cl ion that forms a pair with one I ion in a zigzag structure (Scan area = 15 × 15 Å^2; Sample bias voltage = –2.50 V, Tunneling current = 20 pA). (k) Height profile and bond length of the observed Cl-I zigzag structure in (j). (l) DFT simulated height profile and bond length of the observed Cl-I zigzag structure in (j). Color code for (c), (f), (i) and (l): Pb (dark gray), I (purple), Cl (green), N (brown), C (ice blue), H (light Pink).

is illustrated by the histogram in **Fig 2**, and reveal that the average STM apparent height of the dark protrusions observed in the STM images is about 0.5 ± 0.2 Å lower than the neighbouring iodine ions (**Figs 3d,e and 3j,k**).

To unravel the origin of the dark protrusions observed in the STM images of $MAPbI_3$ after $PbCl_2$ deposition, we performed DFT calculations by using the Vienna *ab initio* simulation package (VASP) (see the **Methods** Section). By tentatively assigning the dark protrusions to Cl ions, we obtained simulated STM images of the Cl-incorporated $MAPbI_3$ surfaces. The simulated images reproduce accurately the dimer and zigzag structures observed experimentally for the $MAPbI_3$ surface (**Fig S3**). Our calculations also reproduce the lowering of the apparent height due to Cl incorporation, which agrees with the experimental STM results (**Figs 3d and 3j**). The incorporated Cl ions in the simulated models were found to be 0.73 - 0.74 Å (**Figs 3f and 3l**) lower than their neighbouring iodine ions, which agrees well with the experimental value of ~0.7 Å in **Figs 3e and 3k** and the average value of 0.5 ± 0.2 Å based on the statistical analyses in **Fig 2**. Also, we found that the experimental bond lengths (d_{Cl-I}) of the Cl-I pairs (~4.9 and ~5.0 Å) in the dimer and zigzag structures (**Figs 3e and 3k**) were 5.11 and 5.69 Å, respectively (**Figs 3f and 3l and Figs S3b and S3e)**, which were also in line with the simulated results**.** Based on the experimental STM data in combination with the DFT calculation and XPS measurement results (**Figs S4-S6**), we can safely conclude the dark protrusions in our STM images of the $MAPbI_3$ surface after 0.5 ML and 0.75 ML of $PbCl_2$ deposition are Cl ions that substitute iodine ions on the perovskite film surface. For simplicity, in the following discussions, we denote Cl-incorporated $MAPbI_3$ as $MAPb(I_{1-x}Cl_x)_3$ with x representing the concentration of Cl ions at the surface.

Based on our STM images, on the surface of $MAPb(I_{1-x}Cl_x)_3$, most Cl ions were observed in the regions close to the grain boundaries and only a few in the center of the grains (**Figs 1d,e and Figs S2b,c**). The substitution of I ions by Cl ions was observed for both the dimer and zigzag structures (**Figs 3d and 3j**). The majority of incorporated Cl ions were found to form Cl-I pairs with neighbouring I ions (see the dashed circles in **Fig 1d,e**). Note that DFT calculations suggest that the dimer structure associated with both the pristine and Cl-incorporated surfaces are more stable than the zigzag one by about 0.030 eV, in good agreement with the energy difference of 0.034 eV reported in a previous study [34]. In addition, the experimental STM images (**Fig 1e**) also show a few incorporated Cl ions bonding together to form the Cl-Cl pairs. The possibility for the appearance of these Cl-Cl pair was also confirmed by DFT calculations, with the simulated STM image (**Fig S7**) reproducing well the Cl-Cl configurations observed in the STM experiments.

Fig 4 shows several configurations for adjacent (**Figs 4a**,**d**) and non-adjacent Cl-I pairs (**Fig 4g**) in the dimer structure observed in STM experiments. DFT calculations verified the possibilities of these configurations (**Figs 4b,c**, 4**e,f**, and 4**h,i**) as well as predicted several other possible configurations for the adjacent and non-adjacent Cl-I pairs in the dimer and zigzag structures, as shown in **Figs S7** and **S8**. Note that these configurations in the dimer **(Figs 4** and **Fig S7**) or zigzag (**Fig S8**) structures have rather close total energies, which rationalizes the variety of configurations for two Cl-I pairs observed in **Fig 4**.

We increased the deposition time of $PbCl_2$ to 12 min to achieve more Cl incorporation in the dimer and zigzag structures, but observed that the $MAPbI_3$ film was completely covered by 1.5 ML of $PbCl_2$ (**Fig 5**). Note that by XPS measurements (**Fig S6**) on the fully covered $MAPbI_3$ surface by $PbCl_2$, we observed a higher Cl concentration in comparison with the samples after a shorter time of $PbCl_2$ deposition. Considering the fact that the 1 min deposition of $PbCl_2$ did not lead to the surface incorporation of Cl ions in the $MAPbI_3$ film, we deduced that the stable Cl surface incorporation should correspond to those samples after 0.5 ML and 0.75 ML deposition of $PbCl_2$. According to the histogram shown in **Fig 2**, the [Cl] : ([Cl] + [I]) concentration of 14.8 ± 0.6% was extracted for the Cl incorporated $MAPbI_3$, i.e., $MAPb(I_{0.85}Cl_{0.15})_3$. However, according to the XPS results (**Fig S5**), the incorporated Cl concentration of 40% was determined, which significantly differs from the concentration extracted from the STM histogram analyses (**Fig 2**). This is possibly because XPS measurements not only probe Cl ions mixed in the top surface layer but also those in sub-surface layers.

We further investigated the influences of the incorporated Cl ions on the electronic properties of $MAPbI_3$ films by UPS and IPES measurements (**Fig 6a**). Based on the UPS and IPES measurement results, the bandgap of the pristine $MAPbI_3$ film was determined to be 1.13 eV. After Cl incorporation with 0.75 ML deposition of $PbCl_2$, the bandgap increased to 1.62 eV (0.49 eV larger than that of the pristine $MAPbI_3$ film), suggesting that the incorporation of Cl ions can effectively tune the electronic properties of $MAPbI_3$ [24 52]. Our STM and XPS results suggest that Cl ions are not only incorporated in the top layer but also the sub-surface layers. To determine the main factor that causes the surface bandgap change, we calculated the bandgaps (**Fig 6b)** of the $MAPbI_3$ surface models with Cl ions being only incorporated in the top one, top two, and top four layers as a function of the incorporation ratio (assuming the same Cl concentration for all the relevant layers when Cl ions are incorporated into multiple layers), as shown in **Fig 6b.** It can be seen that there are no substantial bandgap changes when Cl ions are only mixed into the top layer, being the same as that for Cl-incorporated $MAPbBr_3$ [30]. However, when Cl ions are contained in the sub-surface layers, the bandgap increases fast with the increasing chlorine incorporation concentration. This trend is even clearer in the case of Cl ions being incorporated in the top four layers. This indicates that the bandgap enlargement observed in the experiment is mainly a synergic effect of the Cl incorporation in the multiple surface layers (or in other words, more a multi-layer film effect rather than a surface effect). From **Fig 6b**, we can realize that Cl ions are at least incorporated in the top four layers of the surface model consisting of a total of 8 ML of the perovskite lattice structure (here, we consider the MAI layer as a layer and the PbI_2 layer as another layer), as only under this situation the increase of the bandgap (~0.49 eV)

determined by UPS/IPES measurements can be explained qualitatively. We further calculated the density of states (DOS) for the pristine $MAPbI_3$ surface and that with Cl ions incorporated in the top four layers at the concentration of 18.75%, being quite close to the surface Cl ratio of (14.8% ± 0.6%) determined by STM. The DOS in **Fig 6c** also confirmed that incorporated Cl ions would enlarge the bandgap of $MAPbI_3$ by 0.2 eV as a result of the upward and downward shift of the valance and conduction band edges, respectively (**Fig 6c**). In addition, perovskite surface bandgap combined with the analyses of energy level alignments (**Fig S9**) plays a key role in perovskite solar cells [53] (Supplementary Section 1).

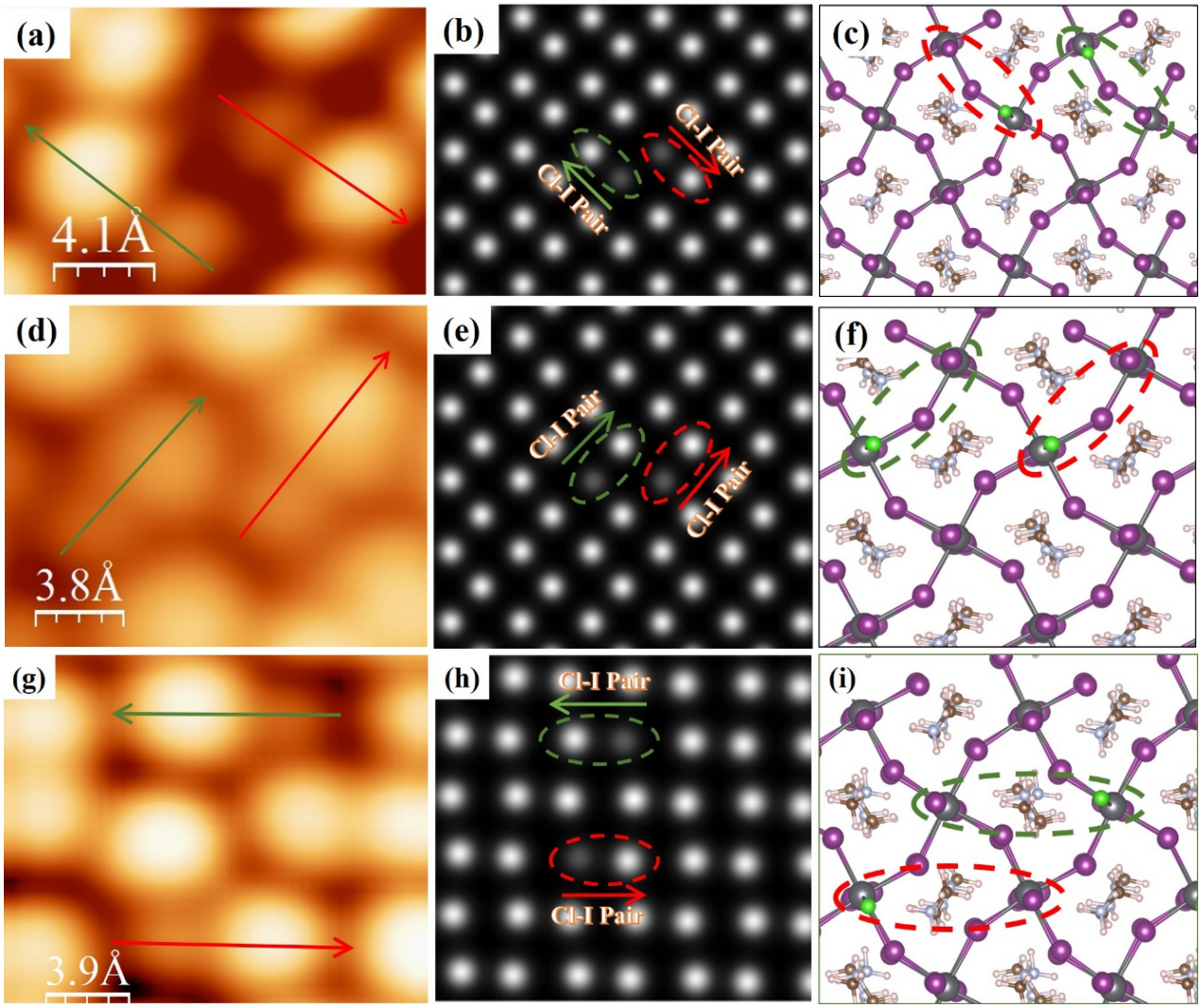

Fig 4. STM images of different configurations of Cl-I pairs in the dimer structure. (a) High-resolution STM image of two adjacent Cl-I pairs with opposite directions; arrows indicate the direction from Cl to I ion in the dimer (Scan area = 1×1.6 nm^2; Sample bias voltage = –2.50 V, Tunneling current = 30 pA). (b-c) Simulated STM image and atomic model for the two Cl-I pairs observed in (a). (d) High-resolution STM image of two adjacent Cl-I pairs showing the same parallel orientation; arrows indicate the direction from Cl to I ion in the dimer (Scan area = 1.4×1.8 nm^2; Sample bias voltage = –2.50 V, Tunneling current = 30 pA) in two parallel dimers in the small grain in Fig 1 (d-e). (e-f) Simulated STM image and atomic model for the two Cl-I pairs observed in (d). (g) High-resolution STM image of two non-adjacent Cl-I pairs with opposite directions (Scan area = 1.7 ×2 nm^2; Sample bias voltage = –2.50 V, Tunneling current = 30 pA) (h-i) Simulated STM image and atomic model for the two Cl-I pairs observed in (g). Color code for (c), (f), and (i): Pb (dark gray), I (purple), Cl (green), N (brown), C (ice blue), H (light Pink).

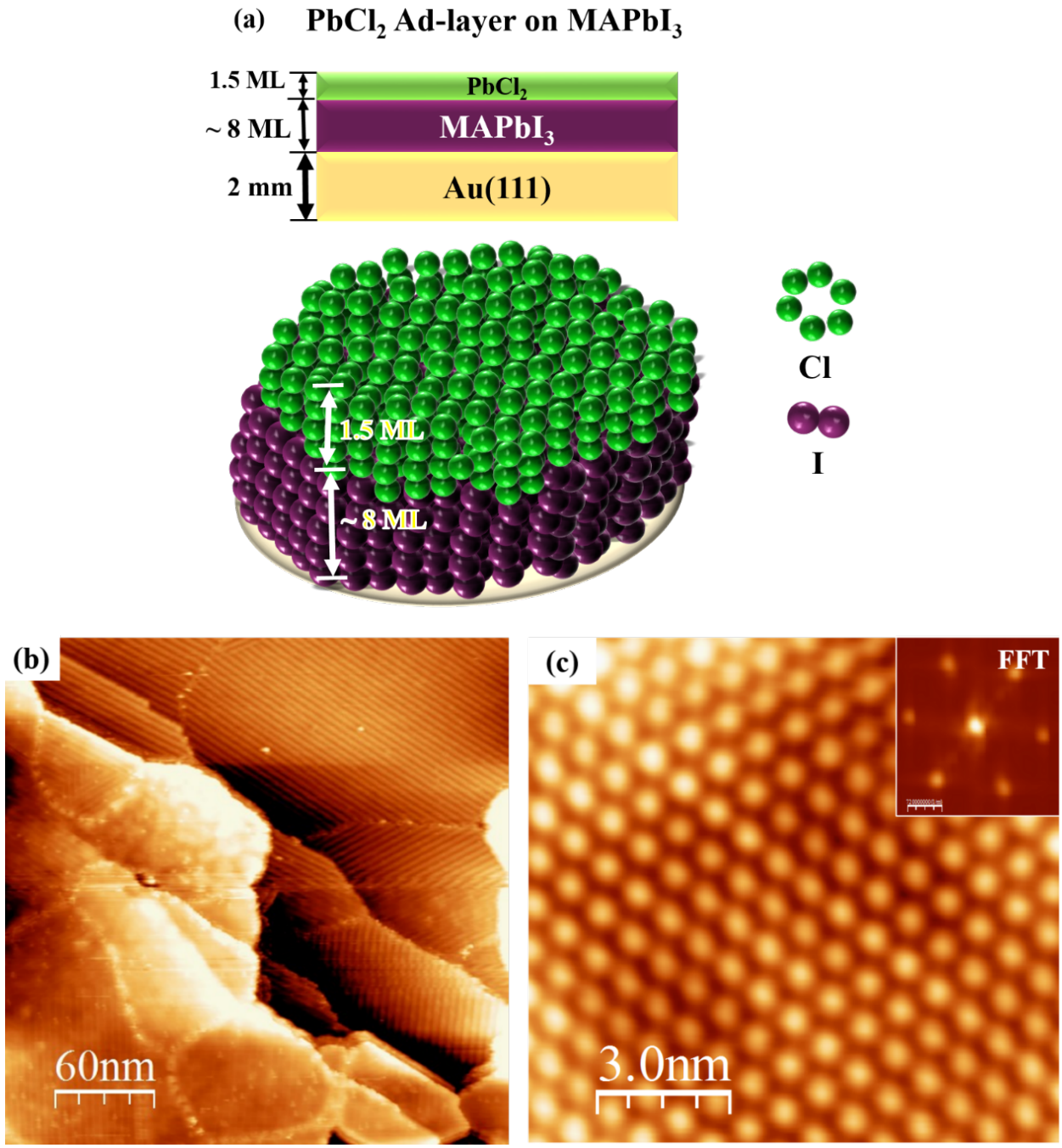

Fig 5. Atomic model and STM high-resolution images of the $MAPbI_3$ thin film after 1.5 ML of $PbCl_2$ deposition. (a) Atomic model configuration of 1.5 ML $PbCl_2$ ad-layer on $MAPbI_3$. (b) Large area STM topography image of $PbCl_2$ fully covering the $MAPbI_3$ thin film (Scan area = 300 × 300 nm^2, Sample bias voltage = –2.50 V, Tunnelling current = 400 pA). (c) High-resolution STM image of the $PbCl_2$ surface structure located in the centre of a grain. (Scan area = 13 × 15 nm^2 (Sample bias voltage = –2.50 V, Tunnelling current = 400 pA). Inset shows the fast Fourier transform (FFT) image indicating the hexagonal structure of $PbCl_2$.

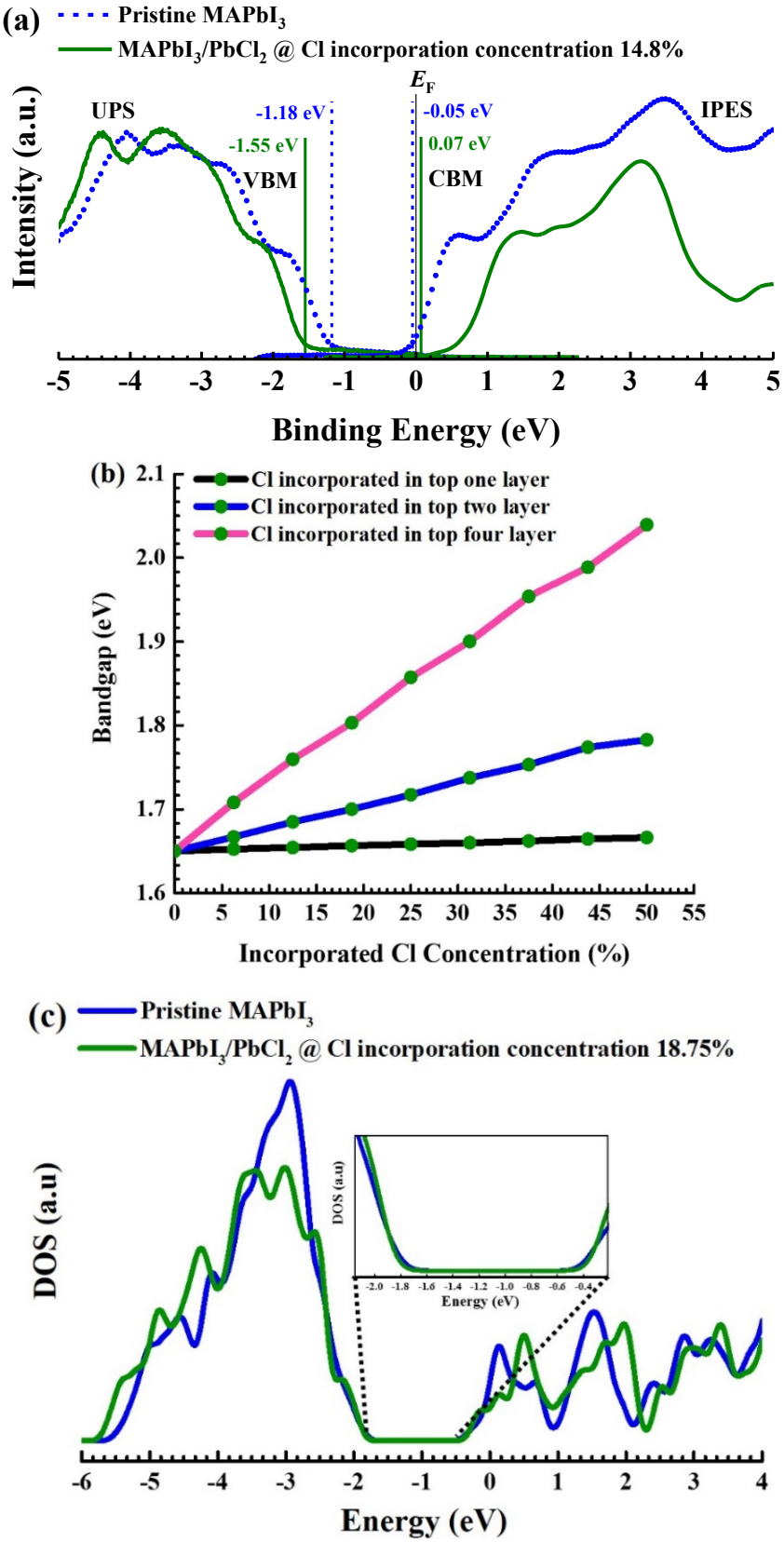

Fig 6. Experimental and DFT calculated bandgap of pristine and Cl incorporated $MAPbI_3$ (a) Experimental ultraviolet and inverse photoemission spectroscopy (UPS-IPES) spectra of the pristine (dashed blue curves) and Cl-incorporated (solid green curves) $MAPbI_3$ surfaces. (b) Calculated bandgaps of the $MAPbI_3$ surface model with Cl ions only being incorporated in the dimer structure in the top one (black), top two (blue), and top four layers (pink) as a function of the incorporation ratio. (c) Calculated DOS of the pristine and Cl-incorporated $MAPbI_3$ surfaces. For the latter, Cl ions are incorporated into the top four layers of the model at the [Cl] : ([Cl] + [I]) concentration of 18.75%. VBM=Valence band maximum, CBM= Conduction band minimum. A larger bandgap was observed after Cl incorporation.

Previous studies have suggested that Cl incorporation can increase the stability of perovskite materials and solar cell devices [30, 54]. Therefore, to unravel the origin of the enhanced stability of the Cl-incorporated $MAPbI_3$ surface, we evaluated the changes in the decomposition energy (see the **Methods** section) of the $MAPb(I_{1-x}Cl_x)_3$ film for different Cl incorporation concentrations through DFT calculations. Here, we consider two different incorporation modes: (1) Cl ions only being incorporated in the top layer of the surface, corresponding to **Fig 7a**; (2) Cl ions only being incorporated in the second layer, corresponding to **Fig 7b.** It is noticed that upon increasing the incorporated Cl amount, the decomposition energy profiles for both incorporation modes show firstly an increase, and then a decrease. The increase of the decomposition energy is related to the stronger bond strength of Cl-Pb compared to that of I-Pb [55-56]. This bond strength originates from the radius of Cl^- being smaller than that of I^-, causing a shorter bond length and in turn a stronger electrostatic interaction between bonded Cl^- and Pb^{2+} than that between bonded I^- and Pb^{2+}. However, the incorporation of the smaller Cl^- ion in the inorganic lattice of $MAPbI_3$ also induces the strain, which in turn pushes up the total energy of the system. At low Cl concentrations (i.e., below 18.75%), the influence of the strain on the total energy of the system is not predominant. But when the Cl concentration exceeds a threshold, the strain overrides the benefit of the stronger Cl–Pb bond, leading to the reduction in the decomposition energy. An increase of the decomposition energy with low concentrations of Cl incorporation suggests higher stability of the $MAPbI_3$ film concerning external stimuli such as temperature or X-ray beams [57]. Also, it is found that the maximum increase of the decomposition energy for the incorporation in the second layer (**Fig 7b)** is 0.08 eV larger than that for the incorporation in the top layer (**Fig 7a**), which indicates that Cl ions mixed into the sub-surface layers play a more significant role in stabilizing the $MAPbI_3$ surface than those in the top layer alone.

In **Fig 7b,** the predicted optimal incorporation concentration of Cl into the second layer is 25%, being noticeably higher than that of the top layer (18.75%), which is consistent with our XPS measurements showing that the concentration in the sub-surface layers is higher than that in the top layer. These results also suggest that the Cl^- ions in the top-most surface layer can diffuse into the subsurface layers of the $MAPbI_3$ ultra-thin film. We can also understand this experimental finding from the viewpoint of energy according to **Fig 7**. From Eq. (3) in the **Methods** section, we can know that at a fixed incorporated chlorine concentration, the higher decomposition energy corresponds to the lower total energy of $MAPb(I_{1-x}Cl_x)_3$. It can be seen from **Fig 7** that when the incorporated concentration is less than ~40%, the total energy of $MAPb(I_{1-x}Cl_x)_3$ with the incorporation in the second layer is lower than that with the incorporation in the top layer, indicating that Cl ions prefer to stay in the sub-surface layers. This finding is consistent with the experimental observation that the incorporated Cl concentration in the sub-surface layers is higher than that in the top layer. Moreover, it is found that the decomposition energies within the positive range of both the dimer and zigzag structures differ negligibly, which corroborates the experimental observation of Cl ions incorporated in the surface structure with the dimer and zigzag structures simultaneously. Last but not least, when the incorporated [Cl] : ([Cl] + [I]) concentration is higher than ~25% for incorporation in the top layer and higher than ~40% for incorporation in the second layer, the decomposition energy of $MAPb(I_{1-x}Cl_x)_3$ becomes negative, meaning that $MAPb(I_{1-x}Cl_x)_3$ cannot exist stably, which determines in principle that the incorporated concentration for stable $MAPb(I_{1-x}Cl_x)_3$ samples will not exceed 25% in the top layer and 40% in the second layer. These predicted upper limits are consistent with our experimental results showing the incorporated Cl concentration of 14.8±0.6% in the top layer and 40% on average in several other sub-surface layers.

To further understand the influence of Cl ions on the stability of Cl-incorporated $MAPbI_3$ surfaces, we also calculated the surface energies of the pristine $MAPbI_3$ surface and that with one I^- being substituted by Cl^- in the top layer (see **Methods** section), which are summarized in **Table 1**. Note that the incorporation of one Cl atom in the $MAPbI_3$ surface leads to a surface energy decrease of 76 meV and 71 meV for the dimer and zigzag structures, respectively (**Table 1**), which can also explain the stabilization effect of Cl ions on the $MAPbI_3$ surfaces. Also, we performed molecular dynamics (MD) simulations of pristine and Cl-incorporated $MAPbI_3$ surfaces with the dimer structure to examine the impact of Cl ions on the vibration of I and Pb atoms in the top and second layer, by calculating the average moving distances for Pb and I atoms during the 1 ps MD simulation, which are shown in **Table 2.**

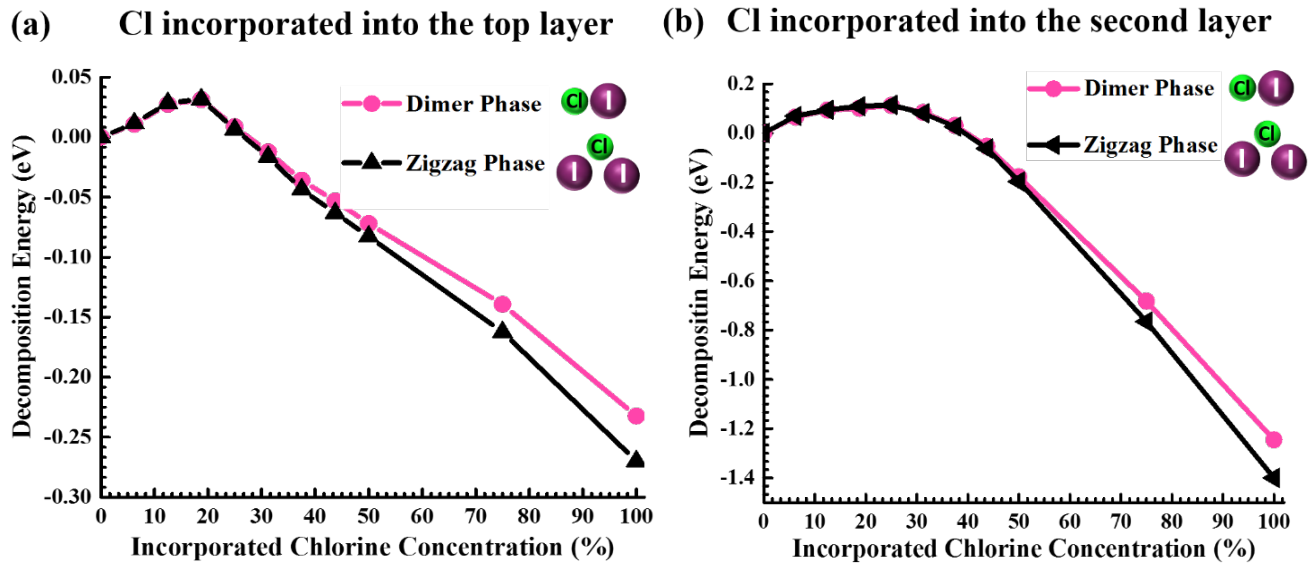

Fig 7. The decomposition energy difference between the pristine and Cl-incorporated $MAPbI_3$ surface determined by DFT calculations (see Methods section): (a) Cl ions only incorporated in the top layer, and (b) Cl ions only incorporated in the second layer.

Table 1: Calculated surface energy (in eV) of the pristine and Cl-incorporated $MAPbI_3$ surfaces in the dimer and zigzag structures.

Perovskite	Dimer	Zigzag
$MAPbI_3$	6.354	6.385
$MAPb(I_{1-x}Cl_x)_3$	6.278	6.314

Table 2: The average moving distances for the I ion in the first layer (d_{I1}) and that in the second layer (d_{I2}) and the Pb ion in the second layer (d_{Pb}) during 1 ps MD simulation.

	$MAPbI_3$	$MAPb(I_{1-x}Cl_x)_3$ (One Cl atom in the first Layer)	$MAPb(I_{1-x}Cl_x)_3$ (One Cl atom in the second Layer)
d_{I1} (Å)	2.477	2.475	2.428
d_{I2} (Å)	2.605	2.481	2.336
d_{Pb} (Å)	2.009	2.008	1.934

These results allow us to analyse the stabilization effect of incorporated Cl ions on the $MAPbI_3$ surface from the viewpoint of kinetics. It is noticed that the incorporation of one Cl ion in the top or second layer suppresses the vibration of Pb and I ions in the 1st and 2nd layer of the surface (**Fig S3**). The weaker vibration of the inorganic lattice will to some extent suppress the diffusion of some intrinsic defects, such as iodine vacancy and interstitial defects, which contributes to the improved stability of $MAPb(I_{1-x}Cl_x)_3$ surfaces. It is interesting to point out that the Cl ion incorporated in the second layer generates a more obvious impact on lowering the vibration strength of Pb and I atoms than the Cl atom in the top layer, being consistent with the analyses for the decomposition energy in **Fig 7.** In conclusion, our DFT calculations verify that the incorporation of Cl ions indeed stabilizes the $MAPbI_3$ surface from the viewpoints of both thermodynamics and kinetics.

Conclusions

In this work, we determined the atomic-scale structure of the Cl incorporated $MAPbI_3$ surfaces. It is found that Cl ions are incorporated in both the $MAPbI_3$ surface and sub-surface layers. Most of the Cl ions incorporated on the surface were found close to the grain boundaries, but some are also found at the centre of the grains for both the dimer and zigzag structures of $MAPbI_3$. Additionally, our XPS measurement results confirm that Cl ions are not present at the surface of $MAPbI_3$ with a short time of $PbCl_2$ deposition, and with a sufficiently long time of $PbCl_2$ deposition (e.g., 12min), the $MAPbI_3$ surface is fully covered by $PbCl_2$. Moreover, the surface bandgap of $MAPbI_3$ is found to be increased by approximately 0.49 eV from 1.13 eV to 1.62 eV when 0.75 ML of $PbCl_2$ is deposited onto the $MAPbI_3$ surface. DFT calculations also predict the bandgap increase observed in the experiment at a similar Cl concentration, and suggests that the incorporation of Cl in the subsurface layers is found to have a stronger impact on the bandgap with respect to Cl ion substitution at only the topmost surface layer. Furthermore, DFT and MD calculations reveal a strong increase of the perovskite stability for low Cl concentrations (below 18.75%). The increase of stability is even more pronounced when substituting the Cl ions in the subsurface layer with respect to the top surface layer. The perovskite material was found to be stabilized both thermodynamically and kinetically. Our findings provide insights into further understanding of the perovskite material and rational design of future high stability perovskite solar cells.

Methods

A. Surface Characterization

Cl incorporated $MAPbI_3$ ultra-thin films on clean Au (111) were studied in an ultrahigh vacuum (UHV) system by STM (base pressure < 2×10^{-10} Torr). Au (111) single crystals was used as the substrates following our previous study[32]. First, the Au (111) substrate was cleaned in UHV conditions by three cycles of Ne^+ sputtering (7.5 x 10^{-5} Torr; 60 min) followed by annealing at 773 K for 20 min. $MAPbI_3$ perovskite films were prepared by co-evaporating PbI_2 and MAI precursors at the temperatures of 516 K and 395 K, respectively, for 3 min. During the co-deposition of PbI_2 and MAI, the Au (111) substrate was kept at a temperature of 132 K to ensure a high sticking coefficient of MAI. After evaporation, the sample was annealed at room temperature for 3 h. This protocol leads to $MAPbI_3$ films with a thickness of ~4-5 nm and with typical grain sizes ranging from 8 nm to 15 nm (Fig S1a). Cl incorporated $MAPbI_3$ samples were obtained by evaporating $PbCl_2$ for a certain duration of time (namely, 1 min, 4 min, 6 min, and 12 min) on top of the pristine $MAPbI_3$ film on the Au (111) substrate. The halide ion exchange reaction takes place according to the following equation:

$$\mathrm{MAPbI_3} + \frac{3x}{2}\mathrm{PbCl_2} \rightarrow \mathrm{MAPb(I_{1-x}Cl_x)_3} + \frac{3x}{2}PbI_2 \quad (1)$$

The samples were *in situ* transferred to a low-temperature scanning tunneling microscope (LT-STM, Scienta Omicron GmbH) for measurements. The STM measurements were performed at 77 K using Pt/Ir STM tips and with the bias voltage applied to the sample. After the STM measurements, the samples were *in situ* transferred to the analysis chamber (the base pressure ~ 2×10^{-10} Torr) equipped with a hemispherical electron energy analyzer (EA 125, Scienta Omicron GmbH), a He discharge lamp (HIS 13, Scienta Omicron GmbH; He-Iα = 21.22 eV) with an energy resolution of ~0.15 eV for UPS measurements, and a dual-anode (Al-Kα = 1486.6 eV and Mg-Kα = 1253.6 eV) non-monochromatic X-ray source (DAR 400, Scienta Omicron GmbH) with an energy resolution of ~0.8 eV for XPS measurements. IPES (LE-1, ALS Technology Co., Ltd.) [58] measurements were performed in a separate vacuum system, and the sample transfer was conducted with the aid of a custom-designed vacuum suitcase (Ferrovac GmbH), which ensures no ambient exposure during sample transfer. For the quantitative analyses of the peak positions, line widths, and relative areas of the Pb 4f, I 3d, C 1s, N 1s, and Cl 2p XPS data, the raw XPS spectra were fitted with Gaussian-Lorentzian functions using the CASA XPS software.

B. Density Functional Theory

Density functional theory (DFT) calculations were performed by using the VASP code [59] with the standard frozen-core projector augmented-wave (PAW) method[60] and the Perdew–Burke–Ernzerhof (PBE) exchange-correlation functional [61]. For the plane-waves, a cutoff of 450 eV was employed. The nonlocal van der Waals interactions were considered by using the Becke–Jonson damping DFT-D3 method [62]. No spin-orbital coupling (SOC) was considered in this work. The lattice parameters (a = 8.84 Å, b = 8.47 Å, and c = 12.65 Å) of the $MAPbI_3$ unit cell in the orthorhombic phase were achieved through structural relaxation with adopting a 4 × 4 × 4 Monkhorst–Pack grid. The $MAPbI_3$ (010) surfaces were modeled by using the 2 × 2 slabs with a vacuum thickness of 20 Å. Each surface model contained eight atomic layers, among which the bottom four layers were always kept fixed at their bulk positions and the other layers were fully relaxed until the atomic forces converged within 0.01 eV/Å (**Fig S3**). For all calculations involving the surfaces, the Brillouin zone was sampled at the sole Γ-point. From the electronic ground state structure, STM images were obtained by using the p4vasp code. All MD simulations were carried out by using the canonical (NVT) ensemble with the temperature being controlled at 300K through the Nosé-Hoover thermostat. The surface energies (E_s) reported in **Table 1** are calculated by using the following equation:

$$E_s = E_{slab} - E_{bulk}, \quad (2)$$

Where E_{slab} is the total energy of the relaxed surface model and E_{bulk} is the total energy of the relaxed bulk model, which also contains eight atomic layers, like the surface one. To evaluate the stability of Cl incorporated $MAPbI_3$ surface, we consider the following reaction [30] :

$$\mathrm{MAPb(I_{1-x}Cl_x)_3} + \frac{3x}{2}\cdot \mathrm{PbI_2} \rightarrow \mathrm{MAPbI_3} + \frac{3x}{2}\cdot \mathrm{PbCl_2}. \quad (3)$$

Hence, the decomposition energy of $\mathrm{MAPb(I_{1-x}Cl_x)_3}$ is given by:

$$E_{\mathrm{dec}} = E(\mathrm{MAPbI_3}) - E(\mathrm{MAPb(I_{1-x}Cl_x)_3}) + \frac{3x}{2}[E(\mathrm{PbCl_2}) - E(\mathrm{PbI_2})], \quad (4)$$

where $E(\mathrm{MAPbI_3})$ and $E(\mathrm{MAPb(I_{1-x}Cl_x)_3})$ are the total energies of the pristine and Cl-incorporated $MAPbI_3$ surfaces, respectively. For perovskites, decomposition energy is widely used to characterize their stability. The larger decomposition energy implies a more stable structure.

Author Contributions

Y.B.Q. conceived the idea, designed the experiments, and supervised the project. A.J., J.H., C.S., R.O., and L.K.O. performed the STM experiments and data analyses. A.J. and L.K.O. performed the XPS, UPS, and IPES measurements and analyses. Z.G. and W.J. performed the DFT calculations. L.Q. and G.T. provided valuable suggestions. All authors

contributed to writing the paper. A.J. and Z.G. contributed equally to this work.

Conflicts of interest

The authors declare no competing financial interest.

Acknowledgements

This work was supported by funding from the Energy Materials and Surface Sciences Unit of the Okinawa Institute of Science and Technology Graduate University, the OIST R&D Cluster Research Program, the OIST Proof of Concept (POC) Program, the JSPS KAKENHI Grant Number JP18K05266, and JST A-STEP Grant Number JPMJTM20HS, Japan. W. Y. acknowledges the funding support from the National Natural Science Foundation of China (Grant No. 11974257 and 11674237).

References

1. Kojima, A.; Teshima, K.; Shirai, Y.; Miyasaka, T., Organometal Halide Perovskites as Visible-Light Sensitizers for Photovoltaic Cells. *J. Am. Chem. Soc.* **2009,** *131*, 6050.

2. Best Research-Cell Efficiencies, National Renewable Energy Laboratory (NREL), https://www.nrel.gov/pv/assets/pdfs/best-research-cell-efficiencies.20200104.pdf (accessed June 6th, 2021).

3. Li, N.; Niu, X.; Chen, Q.; Zhou, H., Towards commercialization: the operational stability of perovskite solar cells. *Chem. Soc. Rev.* **2020**, 49, 8235-8286.

4. Saliba, M., Polyelemental, Multicomponent Perovskite Semiconductor Libraries through Combinatorial Screening. *Adv. Energy Mater.* **2019,** *9* (25), 1803754.

5. Qiu, L.; He, S.; Ono, L. K.; Qi, Y. B., Progress of Surface Science Studies on ABX_3-Based Metal Halide Perovskite Solar Cells. *Adv. Energy Mater.* **2020**, 1902726.

6. Jeon, N. J.; Noh, J. H.; Yang, W. S.; Kim, Y. C.; Ryu, S.; Seo, J.; Seok, S. I., Compositional engineering of perovskite materials for high-performance solar cells. *Nature* **2015,** *517* (7535), 476-480.

7. Tong, G.; Lan, X.; Song, Z.; Li, G.; Li, H.; Yu, L.; Xu, J.; Jiang, Y.; Sheng, Y.; Shi, Y.; Chen, K., Surface-activation modified perovskite crystallization for improving photovoltaic performance. *Mater. Today Energy* **2017,** *5*, 173-180.

8. Tong, G.; Son, D.-Y.; Ono, L. K.; Liu, Y.; Hu, Y.; Zhang, H.; Jamshaid, A.; Qiu, L.; Liu, Z.; Qi, Y. B., Scalable Fabrication of >90 cm2 Perovskite Solar Modules with >1000 h Operational Stability Based on the Intermediate Phase Strategy. *Adv. Energy Mater.* ***2020***, 10, 2003712.

9. Odysseas Kosmatos, K.; Theofylaktos, L.; Giannakaki, E.; Deligiannis, D.; Konstantakou, M.; Stergiopoulos, T., Methylammonium Chloride: A Key Additive for Highly Efficient, Stable, and Up-Scalable Perovskite Solar Cells. *Energy Environ. Mater.* **2019,** *2* (2), 79-92.

10. Dunlap-Shohl, W. A.; Zhou, Y.; Padture, N. P.; Mitzi, D. B., Synthetic Approaches for Halide Perovskite Thin Films. *Chem. Rev.* **2019,** *119* (5), 3193-3295.

11. Ono, L. K.; Juarez-Perez, E. J.; Qi, Y. B., Progress on Perovskite Materials and Solar Cells with Mixed Cations and Halide Anions. *ACS Appl. Materi. Interfaces* **2017,** *9* (36), 30197-30246.

12. Pool, V. L.; Gold-Parker, A.; McGehee, M. D.; Toney, M. F., Chlorine in $PbCl_2$-Derived Hybrid-Perovskite Solar Absorbers. *Chem. Mater.* **2015,** *27* (21), 7240-7243.

13. Kim, M.; Kim, G.-H.; Lee, T. K.; Choi, I. W.; Choi, H. W.; Jo, Y.; Yoon, Y. J.; Kim, J. W.; Lee, J.; Huh, D.; Lee, H.; Kwak, S. K.; Kim, J. Y.; Kim, D. S., Methylammonium Chloride Induces Intermediate Phase Stabilization for Efficient Perovskite Solar Cells. *Joule* **2019,** *3* (9), 2179-2192.

14. Xu, J.; Boyd, C. C.; Yu, Z. J.; Palmstrom, A. F.; Witter, D. J.; Larson, B. W.; France, R. M.; Werner, J.; Harvey, S. P.; Wolf, E. J.; Weigand, W.; Manzoor, S.; van Hest, M. F. A. M.; Berry, J. J.; Luther, J. M.; Holman, Z. C.; McGehee, M. D., Triple-halide wide–band gap perovskites with suppressed phase segregation for efficient tandems. *Science* **2020,** *367* (6482), 1097-1104.

15. Lee, J.-W.; Park, N.-G., Chemical Approaches for Stabilizing Perovskite Solar Cells. *Adv. Energy Mater.* **2020,** *10* (1), 1903249.

16. Mu, C.; Pan, J.; Feng, S.; Li, Q.; Xu, D., Quantitative Doping of Chlorine in Formamidinium Lead Trihalide ($FAPbI_{3-x}Cl_x$) for Planar Heterojunction Perovskite Solar Cells. *Adv. Energy Mater.* **2017,** *7* (6), 1601297.

17. Wang, K.; Jin, Z.; Liang, L.; Bian, H.; Wang, H.; Feng, J.; Wang, Q.; Liu, S., Chlorine doping for black γ-$CsPbI_3$ solar cells with stabilized efficiency beyond 16%. *Nano Energy* **2019,** *58*, 175-182.

18. Liu, Z.; Ono, L. K.; Qi, Y. B., Additives in metal halide perovskite films and their applications in solar cells. *J. Energy Chem* **2020,** *46*, 215-228.

19. Ng, T.-W.; Chan, C.-Y.; Lo, M.-F.; Guan, Z. Q.; Lee, C.-S., Formation chemistry of perovskites with mixed iodide/chloride content and the implications on charge transport properties. *J. Mater. Chem. A* **2015,** *3* (17), 9081-9085.

20. Wang, M.; Li, B.; Siffalovic, P.; Chen, L.-C.; Cao, G.; Tian, J., Monolayer-like hybrid halide perovskite films prepared by additive engineering without antisolvents for solar cells. *J. Mater. Chem. A* **2018,** *6* (31), 15386-15394.

21. Bouchard, M.; Hilhorst, J.; Pouget, S.; Alam, F.; Mendez, M.; Djurado, D.; Aldakov, D.; Schülli, T.; Reiss, P., Direct Evidence of Chlorine-Induced Preferential Crystalline Orientation in Methylammonium Lead Iodide Perovskites Grown on TiO_2. *J. Am. Chem. Soc.* **2017,** *121* (14), 7596-7602.

22. Muscarella, L. A.; Hutter, E. M.; Sanchez, S.; Dieleman, C. D.; Savenije, T. J.; Hagfeldt, A.; Saliba, M.; Ehrler, B., Crystal Orientation and Grain Size: Do They Determine Optoelectronic Properties of MAPbI3 Perovskite? *J. Phys. Chem. Lett.* **2019,** *10* (20), 6010-6018.

23. Odysseas Kosmatos, K.; Theofylaktos, L.; Giannakaki, E.; Deligiannis, D.; Konstantakou, M.; Stergiopoulos, T., Methylammonium Chloride: A Key Additive for Highly Efficient, Stable, and Up-Scalable Perovskite Solar Cells. *Energy Environ. Sci.* **2019,** *2* (2), 79-92.

24. Li, Y.; Sun, W.; Yan, W.; Ye, S.; Peng, H.; Liu, Z.; Bian, Z.; Huang, C., High-Performance Planar Solar Cells Based On $CH_3NH_3PbI_{3-x}Cl_x$ Perovskites with Determined Chlorine Mole Fraction. *Adv. Funct. Mater.* **2015,** *25* (30), 4867-4873.

25. Zhang, H.; Liao, Q.; Wang, X.; Hu, K.; Yao, J.; Fu, H., Controlled Substitution of Chlorine for Iodine in Single-Crystal Nanofibers of Mixed Perovskite $MAPbI_{3-x}Cl_x$. *Small* **2016,** *12* (28), 3780-3787.

26. Colella, S.; Mosconi, E.; Fedeli, P.; Listorti, A.; Gazza, F.; Orlandi, F.; Ferro, P.; Besagni, T.; Rizzo, A.; Calestani, G.; Gigli, G.; De Angelis, F.; Mosca, R., $MAPbI_{3-x}Cl_x$ Mixed Halide Perovskite for

Hybrid Solar Cells: The Role of Chloride as Dopant on the Transport and Structural Properties. *Chem. Mater.* **2013,** *25* (22), 4613-4618.

27. Yin, W.-J.; Chen, H.; Shi, T.; Wei, S.-H.; Yan, Y., Origin of High Electronic Quality in Structurally Disordered $CH_3NH_3PbI_3$ and the Passivation Effect of Cl and O at Grain Boundaries. *Adv. Electron. Mater.* **2015,** *1* (6), 1500044.

28. Dunlap-Shohl, W. A.; Zhou, Y.; Padture, N. P.; Mitzi, D. B., Synthetic Approaches for Halide Perovskite Thin Films. *Chem. Rev.* **2019,** *119* (5), 3193-3295.

29. Hieulle, J.; Luo, S.; Son, D.-Y.; Jamshaid, A.; Stecker, C.; Liu, Z.; Na, G.; Yang, D.; Ohmann, R.; Ono, L. K.; Zhang, L.; Qi, Y. B., Imaging of the Atomic Structure of All-Inorganic Halide Perovskites. *J. Phys. Chem. Lett.* **2020,** *11, 3*, 818-823.

30. Hieulle, J.; Wang, X.; Stecker, C.; Son, D.-Y.; Qiu, L.; Ohmann, R.; Ono, L. K.; Mugarza, A.; Yan, Y.; Qi, Y. B., Unraveling the Impact of Halide Mixing on Perovskite Stability. *J. Am. Chem. Soc.* **2019,** *141* (8), 3515-3523.

31. Stecker, C.; Liu, K.; Hieulle, J.; Ohmann, R.; Liu, Z.; Ono, L. K.; Wang, G.; Qi, Y. B., Surface Defect Dynamics in Organic–Inorganic Hybrid Perovskites: From Mechanism to Interfacial Properties. *ACS Nano* **2019,** *13* (10), 12127-12136.

32. Ohmann, R.; Ono, L. K.; Kim, H.-S.; Lin, H.; Lee, M. V.; Li, Y.; Park, N.-G.; Qi, Y. B., Real-Space Imaging of the Atomic Structure of Organic–Inorganic Perovskite. *J. Am. Chem. Soc.* **2015,** *137* (51), 16049-16054.

33. She, L.; Liu, M.; Li, X.; Cai, Z.; Zhong, D., Growth and interfacial structure of methylammonium lead iodide thin films on Au(111). *Surf. Sci.* **2017,** *656*, 17-23.

34. She, L.; Liu, M.; Zhong, D., Atomic Structures of $CH_3NH_3PbI_3$ (001) Surfaces. *ACS Nano* **2016,** *10* (1), 1126-1131.

35. Cai, L.; She, L. M.; Qin, H. L.; Xu, L.; Zhong, D. Y., Monolayer methylammonium lead iodide films deposited on Au(111). *Surf. Sci.* **2018,** *675*, 78-82.

36. Hu, Z.; Lin, Z.; Su, J.; Zhang, J.; Chang, J.; Hao, Y., A Review on Energy Band-Gap Engineering for Perovskite Photovoltaics. *Solar RRL* **2019,** *3* (12), 1900304.

37. Li, W.; Tang, J.; Casanova, D.; Prezhdo, O. V., Time-Domain ab Initio Analysis Rationalizes the Unusual Temperature Dependence of Charge Carrier Relaxation in Lead Halide Perovskite. *ACS Energy Lett.* **2018,** *3* (11), 2713-2720.

38. Ono, L. K.; Liu, S.; Qi, Y. B., Reducing Detrimental Defects for High-Performance Metal Halide Perovskite Solar Cells. *Angew. Chem. Int. Ed.* **2020,** *59* (17), 6676-6698.

39. Ambrosio, F.; Meggiolaro, D.; Mosconi, E.; De Angelis, F., Charge localization and trapping at surfaces in lead-iodide perovskites: the role of polarons and defects. *J. Mater. Chem. A* **2020,** *8* (14), 6882-6892.

40. Wang, Qian-Kun, Wang, Rong-Bin, Shen, Peng-Fei, Li, C., Li, Yan-Qing, Liu, Li-Jia, Duhm, S., Tang, Jian-Xin, Energy Level Offsets at Lead Halide Perovskite/Organic Hybrid Interfaces and Their Impacts on Charge Separation. *Adv. Mater. Interfaces*, **2015**, 2, 1400528.

41. Nan, G.; Zhang, X.; Abdi Jalebi, M.; Andaji-Garmaroudi, Z.; Stranks, S.; Lu, G.; Beljonne, D., How Methylammonium Cations and Chlorine Dopants Heal Defects in Lead Iodide Perovskites. *Adv. Energy Mater.* **2018,** *8*, 1702754.

42. Wang, J.; Li, W.; Yin, W.-J., Passivating Detrimental DX Centers in $CH_3NH_3PbI_3$ for Reducing Nonradiative Recombination and Elongating Carrier Lifetime. *Adv. Mater.* **2020,** *32* (6), 1906115.

43. Ono, L. K.; Qi, Y. B., Surface and Interface Aspects of Organometal Halide Perovskite Materials and Solar Cells. *J. Phys. Chem. Lett.* **2016,** *7* (22), 4764-4794.

44. Hawash, Z.; Raga, S. R.; Son, D.-Y.; Ono, L. K.; Park, N.-G.; Qi, Y. B., Interfacial Modification of Perovskite Solar Cells Using an Ultrathin MAI Layer Leads to Enhanced Energy Level Alignment, Efficiencies, and Reproducibility. *J. Phys. Chem. Lett.* **2017,** *8* (17), 3947-3953.

45. Yoo, J. J.; Seo, G.; Chua, M. R.; Park, T. G.; Lu, Y.; Rotermund, F.; Kim, Y.-K.; Moon, C. S.; Jeon, N. J.; Correa-Baena, J.-P.; Bulović, V.; Shin, S. S.; Bawendi, M. G.; Seo, J., Efficient perovskite solar cells via improved carrier management. *Nature* **2021,** *590* (7847), 587-593.

46. Dai, Z.; Yadavalli, S. K.; Chen, M.; Abbaspourtamijani, A.; Qi, Y.; Padture, N. P., Interfacial toughening with self-assembled monolayers enhances perovskite solar cell reliability. *Science* **2021,** *372* (6542), 618.

47. Ralaiarisoa, M.; Busby, Y.; Frisch, J.; Salzmann, I.; Pireaux, J.-J.; Koch, N., Correlation of annealing time with crystal structure, composition, and electronic properties of $CH_3NH_3PbI_{3-x}Cl_x$ mixed-halide perovskite films. *Phys. Chem. Chem. Phys.* **2017,** *19* (1), 828-836.

48. Starr, D. E.; Sadoughi, G.; Handick, E.; Wilks, R. G.; Alsmeier, J. H.; Köhler, L.; Gorgoi, M.; Snaith, H. J.; Bär, M., Direct observation of an inhomogeneous chlorine distribution in $CH_3NH_3PbI_{3-x}Cl_x$ layers: surface depletion and interface enrichment. *Energy Environ. Sci.* **2015,** *8* (5), 1609-1615.

49. Colella, S.; Mosconi, E.; Pellegrino, G.; Alberti, A.; Guerra, V. L. P.; Masi, S.; Listorti, A.; Rizzo, A.; Condorelli, G. G.; De Angelis, F.; Gigli, G., Elusive Presence of Chloride in Mixed Halide Perovskite Solar Cells. *J. Phys. Chem. Lett.* **2014,** *5* (20), 3532-3538.

50. de Quilettes, D. W.; Vorpahl, S. M.; Stranks, S. D.; Nagaoka, H.; Eperon, G. E.; Ziffer, M. E.; Snaith, H. J.; Ginger, D. S., Impact of microstructure on local carrier lifetime in perovskite solar cells. *Science* **2015,** *348* (6235), 683-686.

51. Chae, J.; Dong, Q.; Huang, J.; Centrone, A., Chloride Incorporation Process in $CH_3NH_3PbI_{3-x}Cl_x$ Perovskites via Nanoscale Bandgap Maps. *Nano Lett.* **2015,** *15* (12), 8114-8121.

52. Fang, Y.; Dong, Q.; Shao, Y.; Yuan, Y.; Huang, J., Highly narrowband perovskite single-crystal photodetectors enabled by surface-charge recombination. *Nat. Photonics* **2015,** *9* (10), 679-686.

53. Park, N.-G.; Segawa, H., Research Direction toward Theoretical Efficiency in Perovskite Solar Cells. *ACS Photonics* **2018,** *5* (8), 2970-2977.

54. Zhang, S.; Liu, Z.; Zhang, W.; Jiang, Z.; Chen, W.; Chen, R.; Huang, Y.; Yang, Z.; Zhang, Y.; Han, L.; Chen, W., Barrier Designs in Perovskite Solar Cells for Long-Term Stability. *Adv. Energy Mater.* **2020,** *10* (35), 2001610.

55. Darwent, B. d., Bond dissociation energies in simple molecules, National Standard Reference Data **1970**.

56. Cottrell, T. L., The strengths of chemical bonds. Butterworths Sci. Pub. **1958**.

57. Lu, C.; Choi, I. T.; Woo, M. Y.; Kim, C. K.; Kim, C. H.; Kim, H. K., Well-grown low-defect $MAPbI_{3-x}Cl_x$ films for perovskite solar cells with over 20% efficiency fabricated under controlled ambient humidity conditions. *Electrochim. Acta* **2019,** *326*, 134950.

58. A Yoshida, H., Principle and application of low energy inverse photoemission spectroscopy: A new method for measuring unoccupied states of organic semiconductors. *J. Electron Spectrosc. Relat. Phenom.* **2015**, 204, 116-124.

59. Kresse, G.; Furthmüller, J., Efficient iterative schemes for ab initio total-energy calculations using a plane-wave basis set. *Phys. Rev. B* **1996,** *54* (16), 11169-11186.
60. Kresse, G.; Joubert, D., From ultrasoft pseudopotentials to the projector augmented-wave method. *Phys. Rev. B* **1999,** *59* (3), 1758-1775.
61. Perdew, J. P.; Burke, K.; Ernzerhof, M., Generalized Gradient Approximation Made Simple. *Phys. Rev. Lett.* **1996,** *77* (18), 3865-3868.
62. Grimme, S.; Antony, J.; Ehrlich, S.; Krieg, H., A consistent and accurate ab initio parametrization of density functional dispersion correction (DFT-D) for the 94 elements H-Pu. *J. Chem. Phys.* **2010,** *132* (15), 154104.

Table of Contents

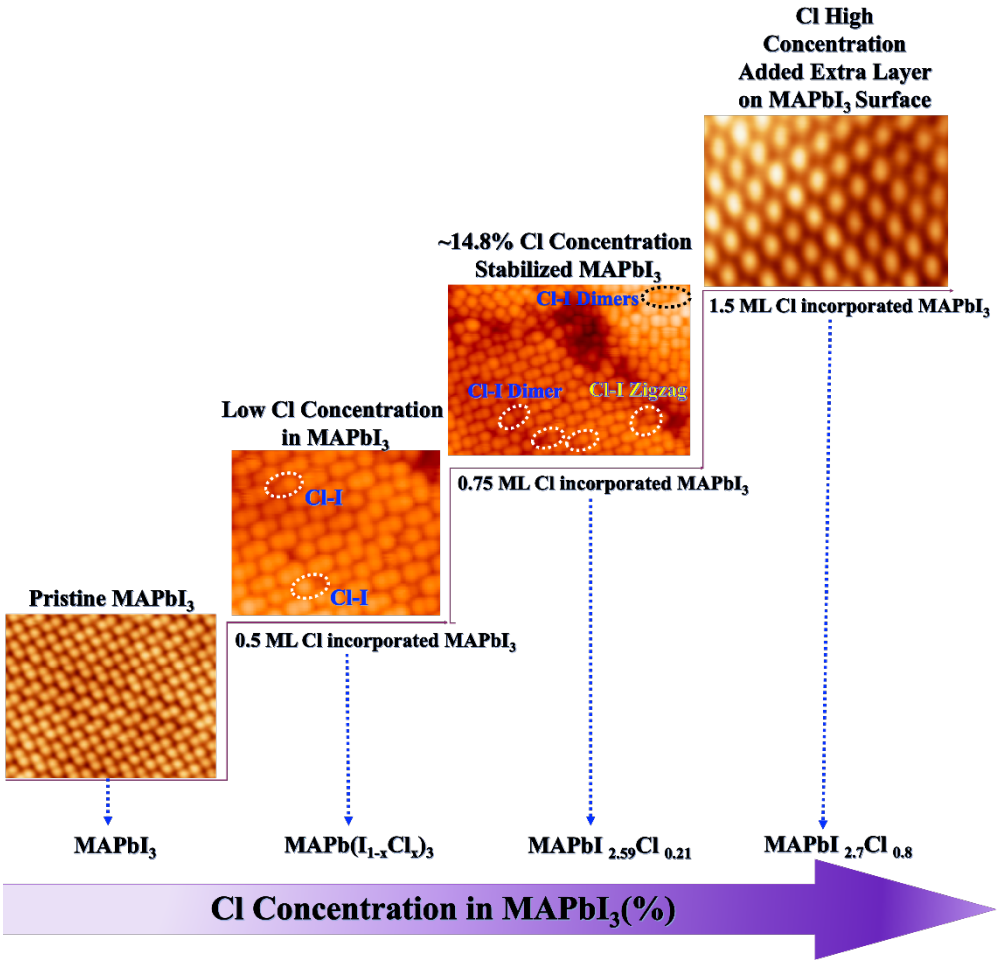

The influence of the Cl incorporation on the structural and electronic properties of metal halide perovskite $CH_3NH_3PbI_3$ is a long-standing puzzle in the field. Cl was found to be an effective strategy to improve the power conversion efficiencies (PCEs) and stability of perovskite solar cells. This study provides a fundamental understanding of the origin of the Cl interactions with perovskite and shows that the Cl concentration plays a crucial role in the surface stability of $MAPbI_3$.